

Deep Neural Networks for Heavy Lepton-Flavor-Violating Higgs Searches at the LHC

Akmal Ferdiyan,^{1,*} Reinard Primulando,^{2,†} Fiki Taufik Akbar,^{1,‡} and Bobby Eka Gunara^{1,§}

¹*Theoretical High Energy Physics Research Division,*

Faculty of Mathematics and Natural Sciences, Institut Teknologi Bandung,

Jl. Ganesha no.10 Bandung, 40132, Indonesia

²*Center for Theoretical Physics, Department of Physics,*

Parahyangan Catholic University, Jalan Ciumbuleuit 94, Bandung 40141, Indonesia

We study lepton-flavor-violating (LFV) decays of a heavy Higgs boson, $H \rightarrow \mu\tau$, in the Type-III two-Higgs-doublet model by recasting the CMS search at $\sqrt{s} = 13$ TeV with 35.9 fb^{-1} using fast detector simulation in the mass range 200–450 GeV. We develop a deep neural network (DNN) classifier trained on final-state kinematic variables that, with mass-dependent threshold optimization, reduces the expected 95% CL upper limits on the signal cross section by 42–46% in the 0-jet channel and 36–40% in the 1-jet channel relative to the standard collinear mass (M_{col}) baseline. We apply SHAP interpretability analysis to identify the visible mass m_{vis} as one of the dominant discriminating feature, reflecting the characteristic neutrino momentum fraction of the τ decay. We show that supplementing the M_{col} analysis with a simplified mass-dependent pre-selection, $m_{\text{vis}} < f \cdot m_H$ with $f = 0.7$ (0-jet) and $f = 0.8$ (1-jet), consistently improves the sensitivity over the M_{col} -only baseline without requiring multivariate infrastructure. In addition, a DNN regression model trained to predict the ratio m_H/M_{col} corrects the systematic prediction bias inherent in the collinear approximation, maintaining an absolute mass prediction error below 1 GeV for signals up to 400 GeV and improving the mass resolution by 12% (0-jet) and 21% (1-jet) at $m_H = 450$ GeV. These results demonstrate a clear path toward significantly enhanced sensitivity in LFV Higgs searches at the LHC.

* aferdiyan@unsoed.ac.id

† rprimulando@unpar.ac.id

‡ ftakbar@itb.ac.id

§ bobby@itb.ac.id

I. INTRODUCTION

The discovery of the 125 GeV Higgs boson at the Large Hadron Collider (LHC) [1, 2] has confirmed the Standard Model (SM) mechanism of electroweak symmetry breaking. The SM, however, remains an incomplete description of nature, failing to account for dark matter, neutrino masses, and the baryon asymmetry of the universe. These shortcomings motivate extensions of the SM, many of which predict lepton flavor violation (LFV) in the Higgs sector. Such LFV interactions, though absent in the SM, arise naturally in two-Higgs-doublet models [3, 4], supersymmetric models [5–7], composite Higgs models [8], models with warped extra dimensions [9, 10], and others [11, 12]. In particular, the Type-III two-Higgs-doublet model (2HDM) provides a minimal and well-motivated framework for generating lepton flavor violation at tree level through the structure of its Yukawa sector [13]. Any observation of LFV Higgs decays would constitute unambiguous evidence of physics beyond the Standard Model.

Searches for LFV decays of the Higgs boson have been carried out by the ATLAS and CMS collaborations. For the 125 GeV Higgs boson, both collaborations have established limits at the $\mathcal{O}(0.1\%)$ level on the branching fractions $\mathcal{B}(h \rightarrow \tau\mu)$ and $\mathcal{B}(h \rightarrow \tau e)$ [14–17], while the constraint on $\mathcal{B}(h \rightarrow \mu e)$ is considerably more stringent, at the $\mathcal{O}(10^{-5})$ level [18, 19]. The search for heavier LFV resonances provides complementary sensitivity and, in the framework of the Type-III 2HDM, can probe a substantially larger region of the parameter space [13]. The CMS collaboration has conducted searches for heavy Higgs decays to $\tau\mu$ and τe in the 200–900 GeV mass range [20], as well as for heavy resonances decaying to μe [18], with the latter reporting a hint of a signal at approximately 146 GeV. No conclusive evidence for LFV Higgs decays has been found in any of these searches.

The existing heavy LFV Higgs searches, involving tau leptons, rely on the collinear mass approximation M_{col} as the primary discriminant. This approximation assumes that the neutrinos from the τ decay are emitted collinear with the visible decay products, and therefore does not exploit the full kinematic information of the final state. Deep neural networks (DNNs) have emerged as powerful tools in the analysis of LHC data [21–24], and have been applied to improve the sensitivity of SM Higgs searches in tau final states [25–27]. However, no attempt has been made to apply these techniques to the search for LFV Higgs decays.

In this paper, we recast the CMS search for heavy LFV Higgs bosons [20] and propose an enhanced analysis framework based on deep learning. We develop a DNN classifier trained on the final-state kinematic variables that achieves a 36–46% reduction in the expected 95% CL upper limits on the signal cross section relative to the M_{col} baseline. In order to interpret the classifier’s decision, we employ SHAP (SHapley Additive exPlanations) [28] values, which identify the visible mass m_{vis} as one of the dominant discriminating

features and lead to a simplified mass-dependent cut that captures a significant fraction of the DNN’s sensitivity gain without requiring multivariate infrastructure. In addition, we develop a DNN regression model that corrects the systematic prediction error inherent in the collinear approximation, maintaining an absolute mass prediction error below 1 GeV for signals up to 400 GeV.

The paper is organized as follows. In Sec. II we give a brief overview of the Type-III 2HDM. In Sec. III we describe the signal and background processes, define the key kinematic variables, and detail the event selection and simulation. The DNN classifier, its interpretability analysis, and the resulting sensitivity limits are presented in Sec. IV. The mass regression study is discussed in Sec. V. We conclude in Sec. VI.

II. TYPE-III TWO-HIGGS-DOUBLET MODEL

Extending the scalar sector of the Standard Model by a second $SU(2)_L$ doublet provides a minimal and well-motivated framework for generating lepton flavor violation at tree level. Unlike the Type-I and Type-II variants, the Type-III two-Higgs-doublet model (2HDM) imposes no discrete symmetry to separate the Yukawa couplings of the two doublets from the fermion sector. As a consequence, both doublets couple simultaneously to all fermion species, and the resulting Yukawa matrices are generically non-diagonal in flavor space [13].

A particularly transparent parametrization of the model is afforded by the Higgs basis [29]. This particular basis had the vacuum structure made manifest by rotating the two doublets, both carrying hypercharge $Y = 1/2$, into a frame where only one of them (Φ_1) acquires a nonzero vacuum expectation value v . The second doublet Φ_2 is inert with respect to electroweak symmetry breaking. In unitary gauge, the two doublets take the form:

$$\Phi_1 = \begin{pmatrix} 0 \\ \frac{1}{\sqrt{2}}(v + \phi_1) \end{pmatrix}, \quad \Phi_2 = \begin{pmatrix} H^+ \\ \frac{1}{\sqrt{2}}(\phi_2 + iA) \end{pmatrix}. \quad (1)$$

The physical mass eigenstates are obtained by diagonalizing the CP-even neutral sector through a rotation by mixing angle α :

$$\begin{pmatrix} \phi_1 \\ \phi_2 \end{pmatrix} = \begin{pmatrix} c_\alpha & s_\alpha \\ -s_\alpha & c_\alpha \end{pmatrix} \begin{pmatrix} h \\ H \end{pmatrix}, \quad (2)$$

where $c_\alpha \equiv \cos \alpha$ and $s_\alpha \equiv \sin \alpha$. The resulting physical spectrum consists of two CP-even neutral scalars h and H (with $m_h < m_H$), one CP-odd neutral scalar A , and a charged scalar pair H^\pm . The lighter state h is

identified with the 125 GeV Higgs boson observed at the LHC, while the heavier state H is the new scalar whose LFV decays are studied in this work.

The Yukawa sector of the model is the key source of phenomenological interest. Fermion masses are generated by Φ_1 through the standard Higgs mechanism, while Φ_2 introduces additional coupling matrices Y_f that need not respect flavor diagonality. The full Yukawa Lagrangian reads [13]:

$$\begin{aligned}\mathcal{L}_{\text{yuk}} = & -\bar{L}_L \frac{\sqrt{2}m_\ell}{v} \ell_R \Phi_1 - \sqrt{2}\bar{L}_L Y_\ell \ell_R \Phi_2 \\ & -\bar{Q}_L \frac{\sqrt{2}m_U}{v} u_R \tilde{\Phi}_1 - \sqrt{2}\bar{Q}_L V Y_u u_R \tilde{\Phi}_2 \\ & -\bar{Q}_L V \frac{\sqrt{2}m_D}{v} d_R \Phi_1 - \sqrt{2}\bar{Q}_L V Y_d d_R \Phi_2,\end{aligned}\quad (3)$$

where m_f are the diagonal fermion mass matrices, Y_f are the generally non-diagonal Yukawa coupling matrices associated with Φ_2 , $\tilde{\Phi} = i\sigma_2\Phi^*$ is the conjugate doublet, and V denotes the Cabibbo–Kobayashi–Maskawa (CKM) matrix. All fermion fields are expressed in the mass eigenbasis, with $SU(2)_L$ doublet assignments:

$$L_L = \begin{pmatrix} \nu_L \\ \ell_L \end{pmatrix}, \quad Q_L = \begin{pmatrix} u_L \\ Vd_L \end{pmatrix}.\quad (4)$$

It is precisely the off-diagonal entries of Y_ℓ that mediate flavor-changing transitions between charged leptons via the exchange of H , A , or H^\pm . In the lepton sector, the coupling of the heavy CP-even scalar H to a $\mu\tau$ pair is proportional to $(Y_\ell)_{\mu\tau}$ and $(Y_\ell)_{\tau\mu}$, making the decay $H \rightarrow \mu\tau$ a direct and clean probe of the off-diagonal Yukawa texture. This decay is the focus of the present analysis.

III. $H \rightarrow \mu\tau$ SEARCH STRATEGY

A. Signal and Backgrounds

We consider the production of H at the LHC via gluon fusion, followed by the LFV decay $H \rightarrow \mu\tau$. The tau lepton subsequently decays either leptonically or hadronically. This study focuses on the leptonic decay mode, $\tau^- \rightarrow e^- \bar{\nu}_e \nu_\tau$, resulting in an opposite-sign pair $e\mu$ and missing transverse energy (E_T^{miss}) in the final state. This channel provides a cleaner experimental signature than the hadronic mode, which requires dedicated τ_h identification algorithms to separate genuine hadronic taus from misidentified quark and gluon jets. The jet $\rightarrow \tau_h$ fake rate and the kinematic properties of the resulting fake candidates are not reliably

reproduced by fast simulation frameworks such as DELPHES [30]. This is because genuine hadronic taus have a distinctive collimated, low-multiplicity structure that the real τ_h identification algorithms exploit, while DELPHES relies on simplified parametric efficiencies that do not capture this substructure. For these reasons, we restrict the present analysis to the leptonic τ decay mode.

The dominant SM background processes contributing to the $e\mu + E_T^{\text{miss}}$ final state are W^+W^- diboson production with leptonic decays of both W bosons, and $t\bar{t}$ production with semi-leptonic decays of both top quarks. The cross sections of additional diboson processes (WZ, ZZ) are smaller by an order of magnitude, and are therefore not included in the present analysis. Other backgrounds such as the $Z \rightarrow \tau\tau$ process, while significant at lower mass scales, this process is suppressed in the search region ($m_H \geq 200$ GeV) the rapidly falling Drell-Yan tail.

B. Event selections

Our work follows the CMS search for $H \rightarrow \mu\tau$ [20], which also serves as the benchmark. Specifically, we investigate the $H \rightarrow \mu\tau_e$ decay channel. The search utilizes 35.9 fb^{-1} of the LHC run data with the corresponding $\sqrt{s} = 13$ TeV. The CMS search requires the events to have two oppositely charged light leptons with different flavors and separated by $\Delta R > 0.3$. The electrons must satisfy the requirements of $p_T > 10$ GeV and $|\eta| < 2.4$; however, events with additional electron candidates with $p_T > 5$ GeV are rejected. The muons are required to have $p_T > 53$ GeV and $|\eta| < 2.4$, and events with additional μ candidates with $p_T > 10$ GeV are likewise rejected. The events are subsequently divided into 0-jet and 1-jet categories. The jets must meet the criteria of $p_T > 30$ GeV and $|\eta| < 4.7$. Events with more than one jet are discarded.

Two mass variables are used extensively in this analysis. The visible mass $m_{\text{vis}} = \sqrt{(p_\mu + p_e)^2}$ is the invariant mass of the muon and electron reconstructed directly from their four-momenta, and systematically underestimates m_H since it ignores the neutrino contributions. The collinear mass $M_{\text{col}} = m_{\text{vis}}/\sqrt{x_\tau}$, where $x_\tau = |\vec{p}_T^e|/(|\vec{p}_T^e| + |\vec{p}_T^{\text{miss}}|)$ is the fraction of the tau momentum carried by the visible decay products, improves upon this by assuming the neutrinos are emitted collinear with the visible tau decay products. While M_{col} provides a better estimate of m_H than m_{vis} in most events, it carries persistent systematic prediction bias arising from the propagation of E_T^{miss} reconstruction uncertainties through the mass formula.

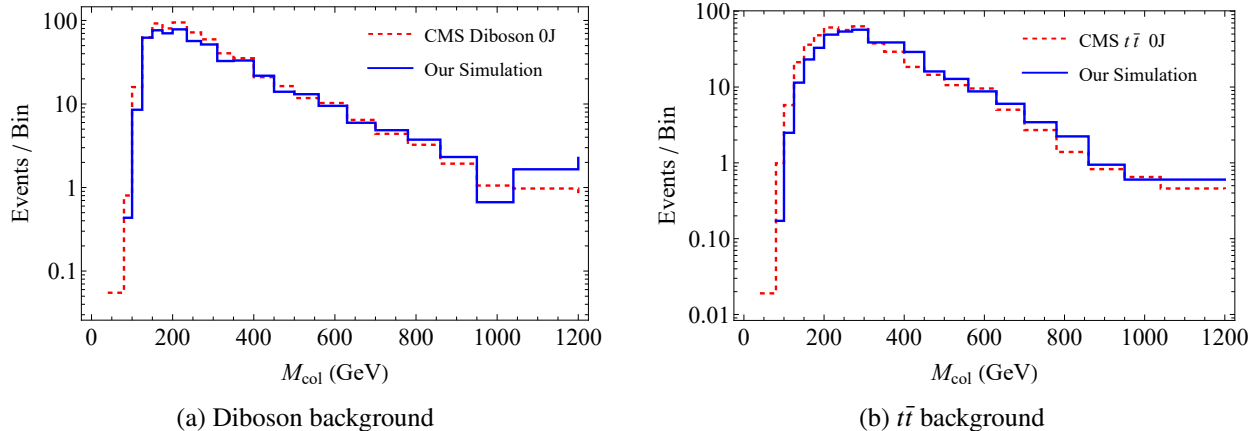


FIG. 1: Validation of simulated background distributions for the 0-jet channel. The distributions of M_{col} for (a) diboson and (b) $t\bar{t}$ processes are compared against the CMS results [20].

C. Simulations and Validations

Signal events for the process $pp \rightarrow H \rightarrow \mu\tau$ with $\tau \rightarrow e\nu_e\nu_\tau$ are generated at leading order using MADGRAPH5 [31] with the SM particle content supplemented by a flavor-violating Yukawa interaction in the Type-III 2HDM framework. Parton showering and hadronization are performed with PYTHIA 8 [32]. A fast detector simulation is carried out with DELPHES 3 [30] employing the CMS detector card. Further analysis, including the extraction of kinematic variables, is performed within the MADANALYSIS 5 framework [33, 34]. To simulate τ decay, we also used the TauDecay library [35] inside the MadGraph framework, to subsequently decay the τ to e, ν_e and ν_τ . The TauDecay package handles the tau decay at the matrix-element level, preserving the spin correlations between the production and decay stages. This ensures that the kinematic features fed to both the classifier and the regression network correctly reflect the polarization state of the tau, which is essential for the validity of the analysis.

To ensure the reliability of our recasting procedure, we performed a rigorous validation of our simulated templates against the official CMS benchmark results. As illustrated in Figs. 1 and 2, the kinematic distributions for the dominant diboson and $t\bar{t}$ backgrounds show close alignment to the CMS predictions across both the 0-jet and 1-jet categories. Similarly, the signal validation for $m_H = 200, 300$ and 450 GeV as shown in Fig. 3 demonstrates that our simulation accurately captures the expected mass resolution and peak positions of the M_{col} variable. This close agreement across all channels establishes a robust foundation for the subsequent DNN-based multivariate analysis and limit-setting procedures.

To provide the DNN with a continuous and dense representation of the signal across the parameter space, signal events were generated in a fine-grained mass scan from 200 GeV to 450 GeV. We sampled 2,000 discrete mass points with a step size of approximately 0.125 GeV. For each mass hypothesis, 1000 events

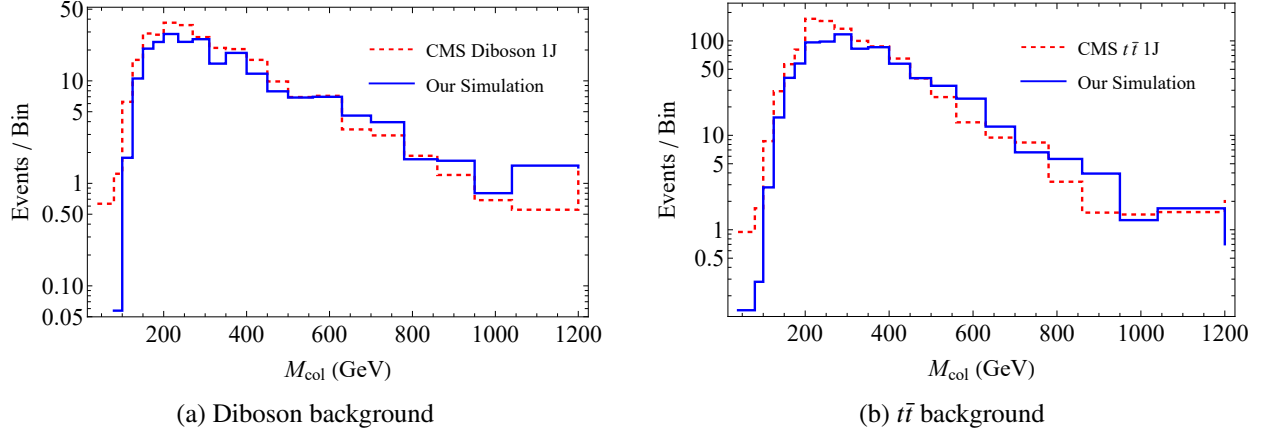


FIG. 2: Validation of simulated background distributions for the 1-jet channel. The distributions of M_{col} for (a) diboson and (b) $t\bar{t}$ processes are compared against the CMS 13 TeV results [20].

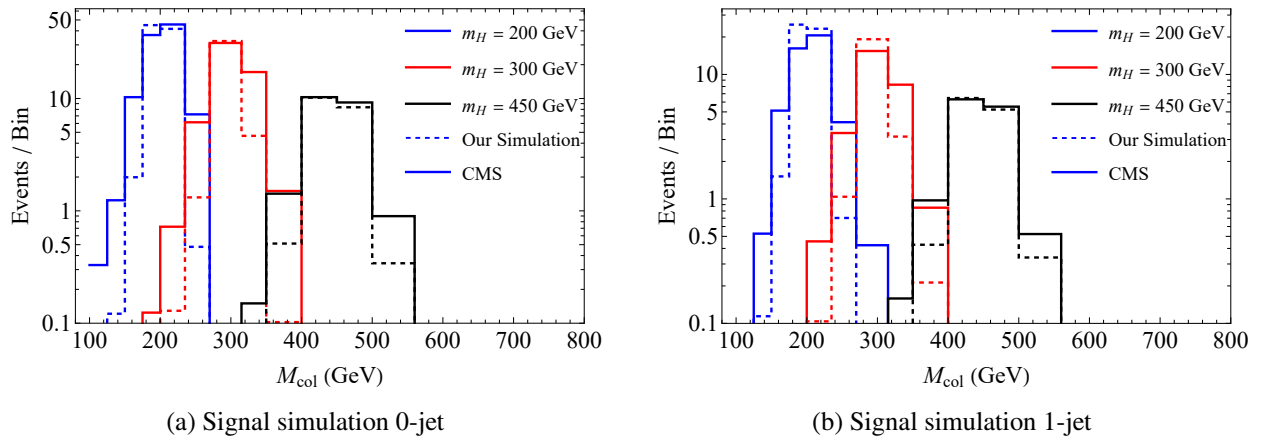


FIG. 3: Signal simulation validation for $m_H = 200, 300$ and 450 GeV. The M_{col} distributions for the 0-jet (a) and 1-jet (b) channels are compared to CMS signal templates [20].

were generated in two independent batches of 500, resulting in a total signal training set of 2×10^6 events. To construct a balanced training dataset and avoid class-imbalance bias, we performed stratified sampling on this signal pool to match the number of background events passing all selection cuts, for both 0-jet and 1-jet categories. Signal events were selected using 50 equal-width bins in the Higgs mass m_H , ensuring a uniform representation of the signal across the entire 200–450 GeV range. This high-density, uniform sampling ensures that the classifier can smoothly interpolate between mass hypotheses and avoids local over-training, while providing the large, quasi-continuous dataset required for the mass regression model described in Sec. V.

IV. DEEP NEURAL NETWORK SIGNAL/BACKGROUND CLASSIFIER

A. DNN architecture and training

Event-level discrimination is performed using ten kinematic features reconstructed from the visible decay products and missing transverse momentum. The input features are the three-momentum components of the muon ($p_x^\mu, p_y^\mu, p_z^\mu$) and electron (p_x^e, p_y^e, p_z^e), the transverse components of the missing momentum (p_x^ν, p_y^ν), the visible mass m_{vis} , and the collinear mass M_{col} , giving a total of ten input features. All features are standardised to zero mean and unit variance prior to training.

The classifier is implemented in TENSORFLOW [36] and trained to distinguish signal events from SM background using binary cross-entropy. The architecture consists of five hidden layers to refine feature representations. In the initial high-capacity layers, Batch Normalization (BN) and Dropout ($p = 0.3$) are applied to stabilize training and reduce neuron co-dependency. To ensure consistent gradient flow across the full dynamic range of the input features, LeakyReLU ($\alpha = 0.1$) is utilized as the activation function throughout all hidden layers. A transitional 32-unit layer is implemented without Batch Normalization, with the purpose of allowing the network to preserve raw activation magnitudes and refine the feature space before the final classification stage. The network's final layer is a Sigmoid output layer, yielding a score $p \in [0, 1]$ where values near unity indicate signal-like events.

Optimization is performed using the Adam algorithm, with a learning rate scheduler and an early stopping criterion (100 epoch patience) ensuring convergence, typically reached within 350 epochs. The characteristic offset between training and validation metrics is a known consequence of the weight-scaling inference rule in Dropout [37] and the shift from mini-batch to population statistics in Batch Normalization [38]. These mechanisms reduce stochastic noise during evaluation, often resulting in validation losses lower than training losses without compromising the model's generalization capabilities.

The full architecture and training configuration are summarised in Tables I and II. Separate models are trained for the 0-jet and 1-jet categories.

To ensure an unbiased evaluation of the DNN performance and the resulting expected limits, the training and testing phases utilize statistically independent datasets. A separate "test-bench" dataset was generated specifically for the sensitivity analysis, consisting of 10^6 events for each primary background process (WW and $t\bar{t}$) and 10^5 events for each signal mass hypothesis. These test samples were produced using independent random seeds and were not seen by the networks during any stage of the training or hyperparameter optimization process. This procedure ensures that the reported results are free from overtraining effects and represent the true generalization power of the multivariate models.

TABLE I: DNN architecture for signal/background classification.

Layer	Units	Activation	Dropout	BN
Input	10	—	—	—
Dense	128	LeakyReLU($\alpha = 0.1$)	0.3	Yes
Dense	64	LeakyReLU($\alpha = 0.1$)	0.3	Yes
Dense	64	LeakyReLU($\alpha = 0.1$)	—	Yes
Dense	32	LeakyReLU	—	No
Dense	32	LeakyReLU($\alpha = 0.1$)	—	Yes
Output	1	Sigmoid	—	—

TABLE II: Training configuration for the signal/background classifier.

Hyperparameter	Value
Optimiser	Adam
Learning rate	10^{-3} , min 10^{-6}
LR scheduler	ReduceLRonPlateau (factor 0.5, patience 10)
Loss function	Binary cross-entropy
Batch size	64
Early stopping	patience 100, monitor val. accuracy
Train/test split	80% / 20% (stratified)
Feature scaling	StandardScaler (zero mean, unit variance)
Input features	$p_x^\mu, p_y^\mu, p_z^\mu, p_x^e, p_y^e, p_z^e, p_x^v, p_y^v, m_{\text{vis}}, M_{\text{col}}$

We evaluate the expected 95 % CL upper limits on the signal cross-section using two distinct strategies. First, we utilize the DNN score $p \in [0, 1]$ as the primary discriminant. Rather than adopting a universal threshold, the cut value p_{cut} is optimized independently for each mass hypothesis by scanning the range $[0.1, 0.99]$. For each threshold, surviving events are binned in M_{col} to calculate the profile likelihood test statistic (Eq. 5),

$$q = 2 \sum_i \left[s_i - b_i \ln \left(1 + \frac{s_i}{b_i} \right) \right], \quad (5)$$

where s_i and b_i are the expected signal and background yields in bin i , normalised to an integrated luminosity of $\mathcal{L} = 35.9 \text{ fb}^{-1}$. The 95% CL limit is obtained by solving $q = 3.84$, corresponding to the one-sided χ^2 critical value for one degree of freedom [39]. The value of p_{cut} minimizing the expected limit is adopted as the optimal working point for each mass hypothesis. In this phenomenological study, we focus on the statistical power of the DNN classifier; therefore, systematic uncertainties on the background normalization and shape are not included in the likelihood fit. The resulting limits represent the maximal potential sensitivity under the fast-simulation framework.

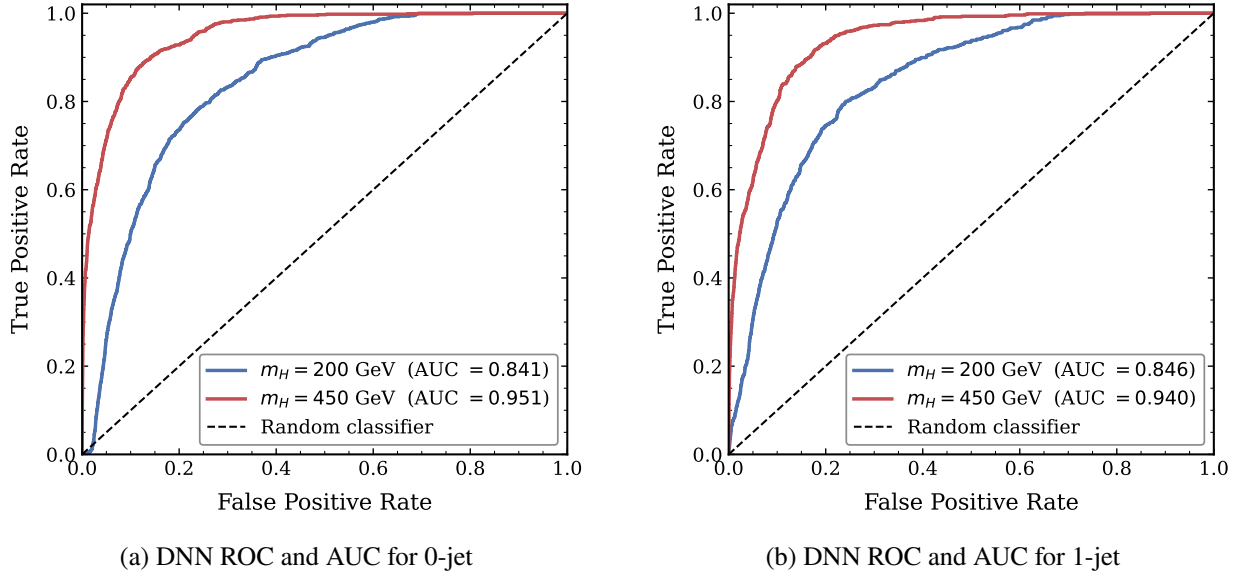


FIG. 4: ROC curves and corresponding AUC values for $m_H = 200$ and 450 GeV, for 0-jet and 1-jet categories. The dashed diagonal line represents the performance of a random classifier (AUC = 0.5). The AUC values demonstrate the increased classification power of the network as the signal mass increases.

To evaluate the model’s performance as a binary classifier, we utilize the Receiver Operating Characteristic (ROC) and Area Under the ROC Curve (AUC), which provides a threshold-independent measure of the network’s ability to discriminate between signal and background. An AUC of 1.0 represents perfect separation, while a value of 0.5 indicates performance no better than random chance. The DNN classifier achieves AUC values of 0.841 (0.846) for $m_H = 200$ GeV and 0.951 (0.940) for $m_H = 450$ GeV in the 0-jet (1-jet) channel, as can be seen in Fig. 4.

The AUC improves with the signal mass in both channels, reflecting the increasingly distinct kinematics of heavier signal events relative to the SM backgrounds. The high AUC values at $m_H = 450$ GeV indicate that the network is particularly effective at separating high-mass signal from background, while the lower AUC at $m_H = 200$ GeV is consistent with the greater kinematic overlap between a 200 GeV resonance and the WW and $t\bar{t}$ backgrounds at low mass. As shown in Fig. 5, the DNN successfully isolates the signal in the high-score region, particularly for heavier mass hypotheses where the boosted kinematics are more distinct. The background concentrates near $p \approx 0$ while the signal populates the high-score region, confirming that the network has learned to discriminate the two hypotheses.

B. Results

The expected 95% CL upper limits on the $H \rightarrow \mu\tau$ production cross-section for the DNN-based and M_{col} baseline methods are presented in Table III and visualized in Fig. 6.

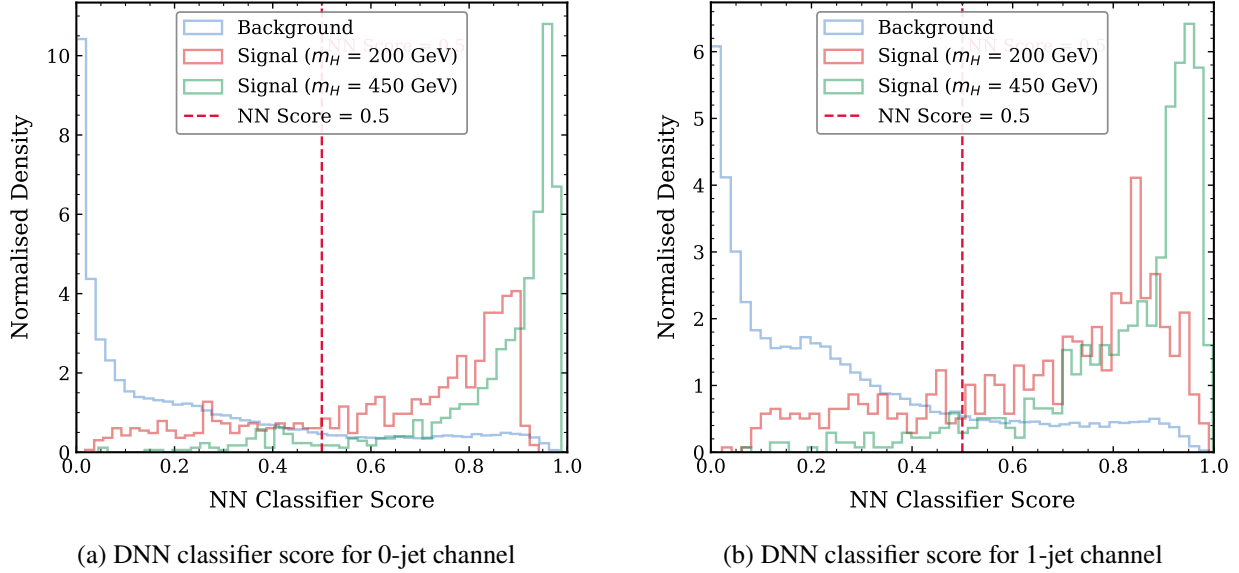


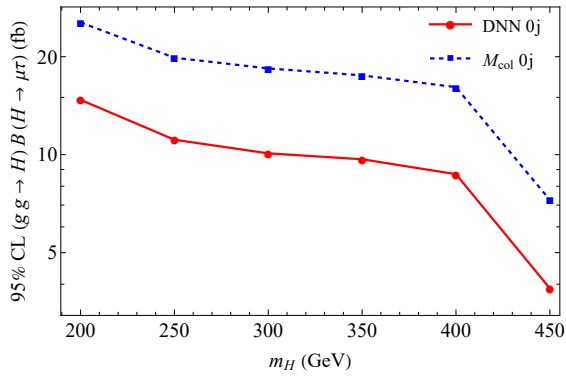
FIG. 5: DNN classifier score distributions for (a) 0-jet and (b) 1-jet channels. The SM background (blue) is compared against signal hypotheses for $m_H = 200$ GeV and 450 GeV (red and green). The clear separation at $p \rightarrow 1$ validates the network’s discriminative power.

In the 0-jet channel, the M_{col} baseline yields limits ranging from 25.50 fb at $m_H = 200$ GeV to 7.26 fb at $m_H = 450$ GeV. The DNN-based selection provides a significant enhancement in sensitivity across the entire mass range, achieving limits of 14.74 fb and 3.88 fb at the same mass points. This represents a 42–46% reduction in the expected upper limits. The sensitivity gain remains stable at intermediate mass points, scaling positively with the signal mass. This trend correlates with the increased boosted topology and higher AUC values at higher m_H . For the 1-jet channel, the M_{col} baseline limits are generally weaker than the 0-jet counterparts at low mass but converge at the high-mass boundary. The DNN selection yields a 36–40% improvement over the baseline. The slightly lower relative gain in the 1-jet channel suggests that additional kinematic complexities partially moderate the classifier’s performance.

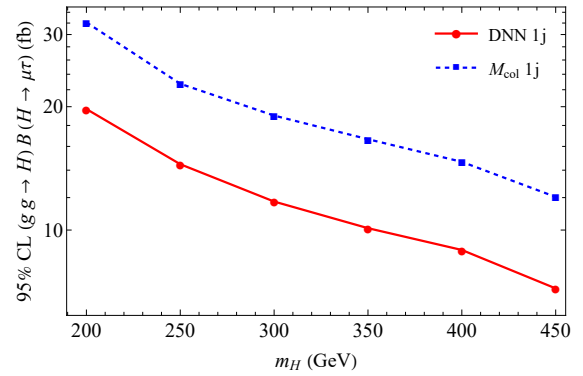
The optimal score threshold (p_{cut}) varies with the signal mass hypothesis. In the 0-jet channel, p_{cut} rises from 0.54 at $m_H = 200$ GeV to a range of 0.82–0.89 for $m_H \in [300, 450]$ GeV. Similarly, in the 1-jet channel, p_{cut} rises from 0.53 at $m_H = 200$ GeV to a plateau of 0.71–0.81 for $m_H \in [250, 450]$ GeV. This behavior reflects the stringent purity requirements optimal for signals that are kinematically well-separated from the background. The combined channel limits (Fig. 6c) demonstrate that the DNN-driven improvements are robust across event categories, consistently outperforming the M_{col} combination.

TABLE III: Expected 95% confidence level upper limits on the signal cross section (fb) obtained using the M_{col} baseline method and the DNN-based analysis in the 0-jet and 1-jet categories.

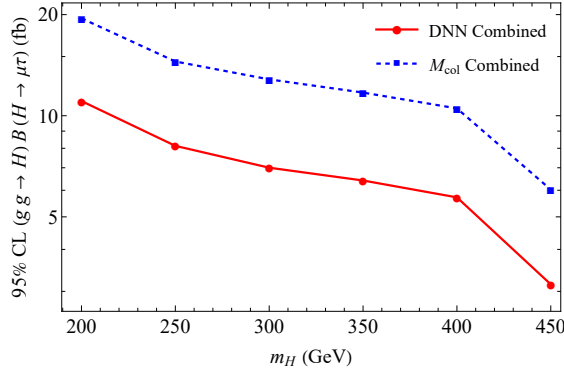
m_H (GeV)	0-jet category			1-jet category		
	M_{col}	p_{cut}	DNN	M_{col}	p_{cut}	DNN
200	25.50	0.54	14.74	32.12	0.53	19.74
250	19.86	0.78	11.11	22.75	0.71	14.48
300	18.41	0.85	10.10	19.03	0.77	11.74
350	17.53	0.86	9.68	16.66	0.81	10.11
400	16.12	0.89	8.71	14.67	0.78	8.94
450	7.26	0.82	3.88	12.04	0.79	7.20



(a) Cross section upper limit for 0-jet



(b) Cross section upper limit for 1-jet



(c) Cross section upper limit, combined channels

FIG. 6: Expected 95 % CL upper limits on the signal cross-section $\sigma(pp \rightarrow H \rightarrow \mu\tau)$ for the (a) 0-jet, (b) 1-jet, and (c) combined channels. The DNN-based limits (red) are compared against the standard M_{col} baseline (blue).

C. Importance Analysis of Kinematic Variables

To interpret the classifier's decision logic, we apply SHAP (SHapley Additive exPlanations) [28] to quantify the contribution of each input feature to the classifier output. As illustrated in Fig.7, where we show

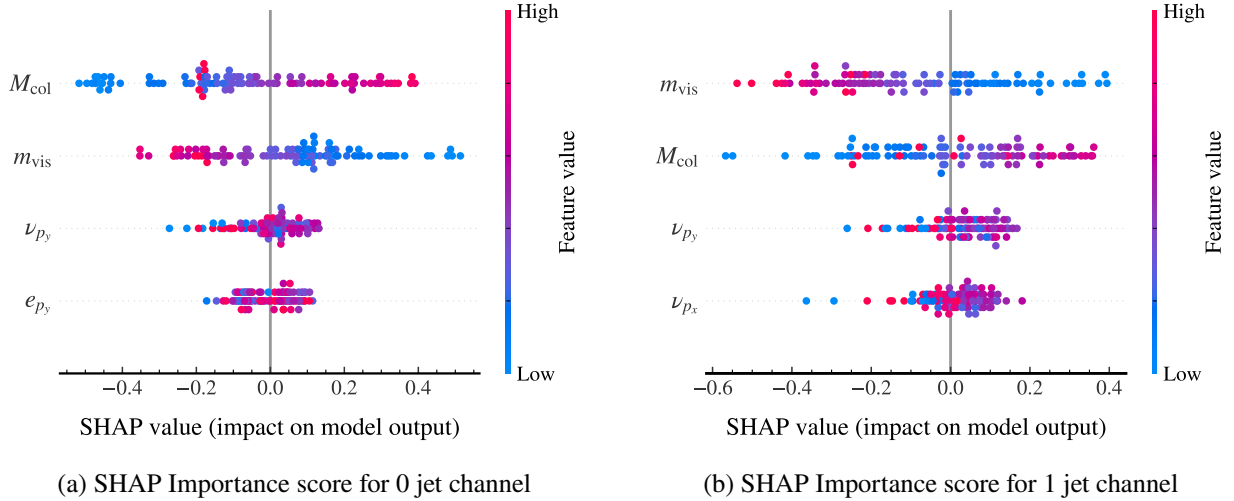


FIG. 7: SHAP summary plot for the Neural Network classifier. Four most important features are ranked by their mean absolute SHAP value, representing their global importance. The color scale indicates the feature value (red for high, blue for low), while the x-axis represents the impact on the model output.

four most important parameters based on SHAP analysis, M_{col} and m_{vis} are the dominant discriminators. While M_{col} shows a strong positive correlation with signal probability—consistent with its role as a mass resonance estimator— m_{vis} exhibits a significant inverse correlation.

The network effectively learns that for an event, a substantial fraction of the tau lepton’s momentum is carried by neutrinos, resulting in m_{vis} values consistently lower than the true m_H . This is visualized in Fig. 8, where the mean DNN score is mapped onto the (m_H, m_{vis}) plane. The resulting gradient demonstrates that the highest signal purity is achieved at large m_H and low m_{vis} . This observation justifies the use of adding a mass-dependent visible mass cut, $m_{\text{vis}} < f \cdot m_H$, as a simplified, yet effective alternative to the full multivariate analysis selection.

Motivated by this observation, we impose a simple additional upper bound on the visible mass as a fraction f of the signal mass hypothesis, where $f \in [0.3, 1.0]$ is scanned in steps of 0.1. No DNN selection is applied; all events passing the visible mass requirement are histogrammed directly in M_{col} . The expected 95% CL upper limit is evaluated using the same test statistic as in Eq. (5), and the value of f minimising the expected limit is adopted for each mass hypothesis.

The resulting limits (Fig. 9) show that this single requirement captures a substantial fraction of the DNN’s sensitivity gain. This result is significant, it demonstrates that the improvement is not merely an algorithmic artifact, but a reflection of a physical kinematic property. Specifically, that the LFV signal consistently exhibits a lower m_{vis}/m_H ratio than the dominant SM backgrounds. While the full DNN remains superior due to its use of the complete ten-dimensional feature space, the m_{vis} cut addition offers a highly interpretable

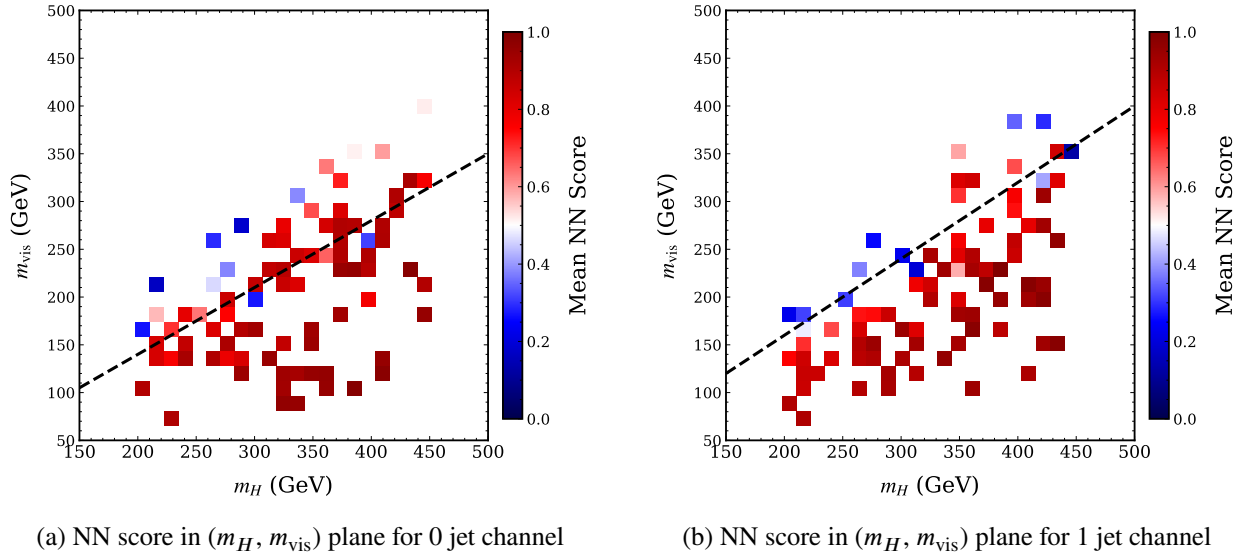


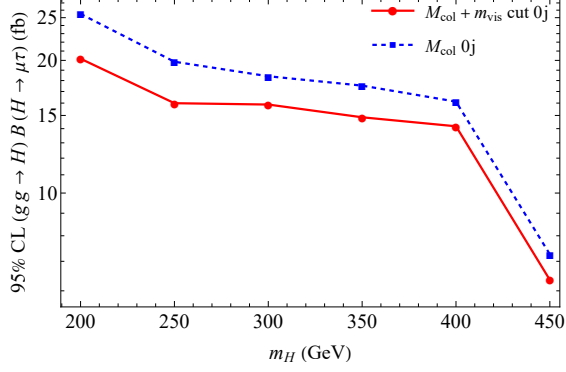
FIG. 8: Mean DNN classifier score projected onto the (m_H, m_{vis}) plane for the (a) 0-jet and (b) 1-jet channels. The color scale represents the signal-like probability, where the gradient illustrates high signal purity at large m_H and low m_{vis} . The dashed black lines represent the mass-dependent selection cuts, $m_{\text{vis}} < 0.7 \cdot m_H$ for the 0-jet channel and $m_{\text{vis}} < 0.8 \cdot m_H$ for the 1-jet channel.

and easily implementable refinement to the standard M_{col} search strategy.

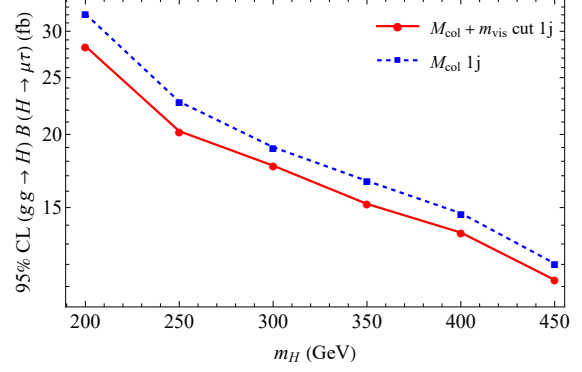
A direct comparison of M_{col} baseline, the M_{col} analysis incorporating an additional m_{vis} cut, and DNN shows a clear hierarchy in sensitivity across the full mass range. The DNN achieves the strongest limits in all cases, followed by the M_{col} analysis with additional m_{vis} cut, while the M_{col} baseline has the lowest sensitivity. The gap between the DNN and the m_{vis} augmented analysis reflects the additional discriminating information captured by the full ten-dimensional input space of the network, beyond what is accessible through m_{vis} alone. Nonetheless, the fact that gain observed by simply adding an m_{vis} cut to the M_{col} baseline remains a significant result. It identifies a concrete and interpretable improvement to the baseline analysis strategy that can be implemented without machine learning infrastructure.

V. MASS RECONSTRUCTION WITH DEEP REGRESSION

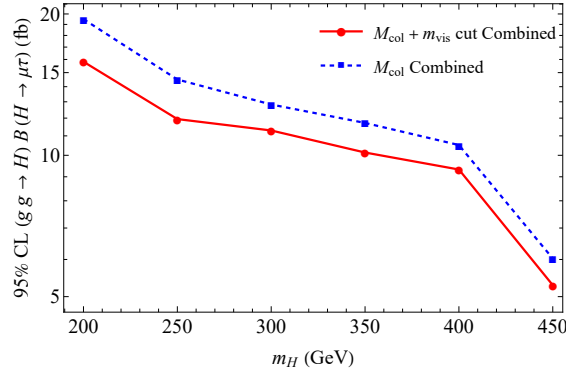
As discussed in Sec. III B, the collinear approximation M_{col} carries an inherent systematic bias arising from the sensitivity of the reconstructed momentum fractions to E_T^{miss} resolution. This limits the M_{col} accuracy and broadens the reconstructed signal resonance. In order to mitigate this limitation, we develop a DNN regression model that learns a data-driven correction to the collinear mass estimate. The regressor takes the same ten input features as the classifier described in Sec. IV. Rather than predicting m_H directly, the network is trained to predict the ratio $R = m_H / M_{\text{col}}$, which is of order unity across the entire mass range



(a) Cross section upper limit for 0-jet, with additional cut on m_{vis}



(b) Cross section upper limit for 1-jet, with additional cut on m_{vis}



(c) Cross section limit, combined channels, with additional cut on m_{vis}

FIG. 9: Comparison of expected 95 % CL upper limits on the signal cross-section $\sigma(pp \rightarrow H \rightarrow \mu\tau)$ using the additional mass-dependent m_{vis} cut (red) against the M_{col} baseline (blue). The m_{vis} requirement significantly enhances the signal-to-background ratio by exploiting the neutrino momentum fraction characteristic of the τ decay.

considered and removes the need to learn the overall mass scale from the raw momenta. The final mass estimate is then recovered as $m_{\text{pred}} = R \cdot M_{\text{col}}$.

For the mass reconstruction task, we use the same high-density signal dataset developed for the DNN classifier, which provides a quasi-continuous representation of the signal across the 200–450 GeV mass range. This allows the network to perform robust mass interpolation and helps prevent overtraining on specific mass hypotheses. We evaluate the model’s generalization on a separate, independent test set consisting of 10 discrete mass points spaced between 200 and 450 GeV. In order to ensure that the performance metrics are not dominated by statistical noise, we generate 10^4 events for each of these test points.

The mass reconstruction model follows the residual architecture described in Fig. 10 and Table IV. We use additive skip connections to allow the network to learn perturbative corrections to the collinear mass while maintaining stable gradient flow during training. In order to handle misreconstructed events in the tails of

the M_{col} distribution, the model is optimized using a Huber loss function ($\delta = 0.1$), which applies a linear penalty to large residuals. This choice, combined with Batch Normalization and LeakyReLU activations, ensures consistent performance and numerical stability across the entire 200–450 GeV mass range.

Training is performed using an early stopping criterion with a patience window of 50 epochs and a dynamic learning rate reduction on plateau; convergence is typically achieved within 150 epochs. To ensure stability against random weight initialization and avoid local minima, the training process is repeated across multiple iterations. The optimal model is subsequently selected using a custom weighted score $S = \sigma_{\text{SD}} + \lambda |\mu - m_H|$, where σ_{SD} is the standard deviation of the predicted mass distribution and $|\mu - m_H|$ represents the prediction bias. We set $\lambda = 50$ to prioritize the minimization of the prediction error over the absolute resolution. The full training configuration is summarized in Table V.

TABLE IV: DNN architecture for mass regression. The model employs residual blocks with Batch Normalization (BN) and LeakyReLU activations. Residual connections (\oplus) denote element-wise addition of the shortcut and processed branches.

Block	Layer Type	Units/Dim.	Activation	Dropout
Input	Feature Vector	10	—	—
Entry	Dense + BN	256	LeakyReLU	0.2
Residual 1	Dense + BN (2 \times)	256	LeakyReLU	0.2
	Shortcut \oplus	256	LeakyReLU	—
Residual 2	Dense + BN (2 \times)	128	LeakyReLU	0.1
	Shortcut \oplus	128	LeakyReLU	—
Output	Fully Connected	1	Linear	—

A. Reconstruction performance

The reconstruction performance is evaluated using three metrics: the prediction error $|\mu - m_H|$, the resolution σ_{SD} , and the normalized pull $|\mu - m_H|/\sigma_{SD}$. The results are shown as a function of m_H in Fig. 11.

In the 0-jet channel, the DNN consistently outperforms M_{col} in terms of prediction error, maintaining an error below 1 GeV for mass points up to 400 GeV, compared to approximately 4.6 GeV for M_{col} at the same mass point. This confirms that the network successfully learns the kinematic correlations required to correct the systematic bias inherent in the collinear approximation, from the E_T^{miss} reconstruction effects. In the 1-jet channel, a similar improvement is observed up to 350 GeV; the crossover at 450 GeV is attributed to boundary effects and limited training statistics at the kinematic edge of the sample.

TABLE V: Training configuration for the mass regression model.

Hyperparameter	Value
Optimizer	Adam
Learning rate	10^{-3} , min 10^{-6}
LR scheduler	ReduceLRonPlateau (factor 0.5, patience 15)
Loss function	Huber ($\delta = 0.1$)
Metric	Mean Absolute Error (MAE)
Batch size	1024
Early stopping	patience 50, monitor val. loss
Train/test split	80% / 20%
Feature scaling	StandardScaler (zero mean, unit variance)
Target variable	m_H/M_{col} (ratio ≈ 1)
Input features	$p_x^\mu, p_y^\mu, p_z^\mu, p_x^e, p_y^e, p_z^e, p_x^\nu, p_y^\nu, m_{\text{vis}}, M_{\text{col}}$

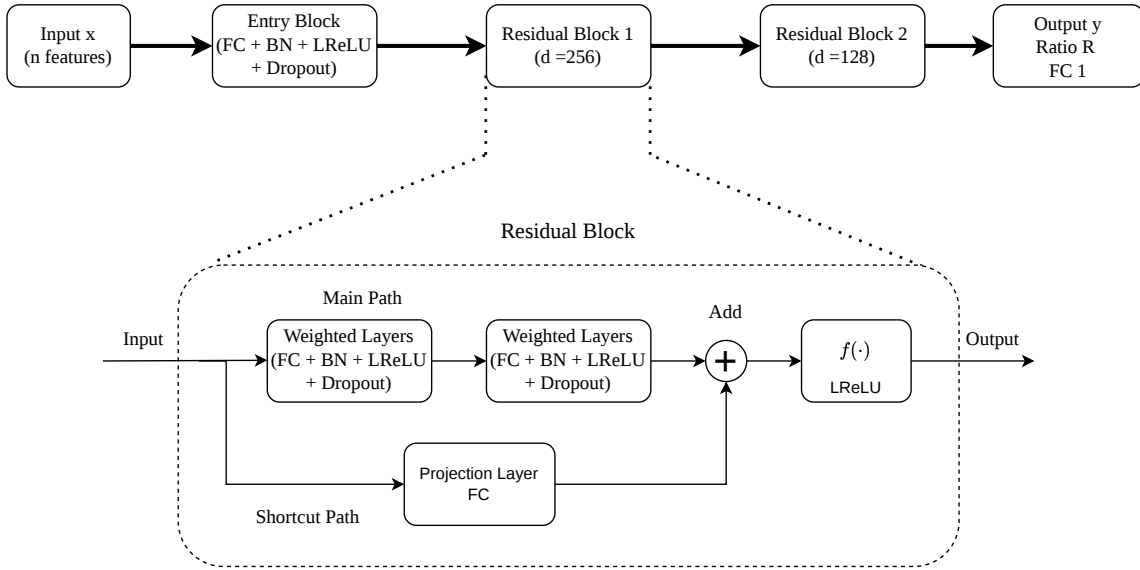


FIG. 10: Schematic of the residual network architecture used for Higgs mass regression. The network consists of an entry block followed by two residual units, each with additive skip connections (\oplus). The activation function $f(\cdot)$ denotes LeakyReLU ($\alpha = 0.1$), applied after each element-wise addition of the shortcut and residual paths.

In terms of resolution, both methods exhibit a characteristic degradation as m_H increases, driven by the scaling of E_T^{miss} and the final-state momenta. However, at the upper boundary ($m_H = 450$ GeV), the DNN provides a relative resolution improvement of 12% (0-jet) and 21% (1-jet) over M_{col} . This suggests that the DNN makes better use of the available kinematic information in the 1-jet category to constrain the neutrino system.

The normalized pull provides the most rigorous metric of reconstruction quality. In the 0-jet channel, the DNN maintains a stable pull below 0.09 across the entire mass range, while the M_{col} pull more than doubles toward the high-mass tail, reaching approximately 0.18. In the 1-jet channel, the DNN pull exhibits non-monotonic behavior, which reflects the varying applicability of the collinear assumption across different boost regimes. The notable exception to the overall improvement is the prediction error in the 1-jet channel at 200 and 450 GeV, where limited training statistics and edge effects cause the DNN to underperform M_{col} ; this is a known limitation and a direction for future improvement [21].

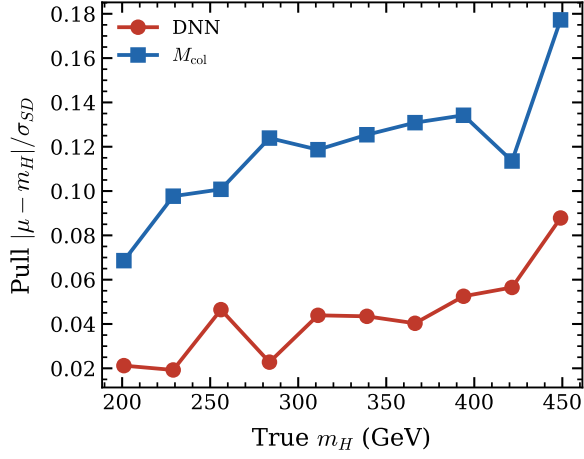
Overall, the DNN regression provides a consistent improvement in mass reconstruction quality relative to the collinear approximation across most of the mass range considered. The most significant gain is in prediction error: the DNN corrects the systematic overestimation of M_{col} at most of considered mass range, maintaining errors below 1 GeV up to 400 GeV in the 0-jet channel, compared to errors exceeding 2 GeV for M_{col} at the same mass points. The normalized pull confirms that the DNN achieves a more accurate and stable reconstruction across the mass spectrum, with the most marked improvement in the 1-jet channel where the collinear approximation is most challenged.

VI. CONCLUSION

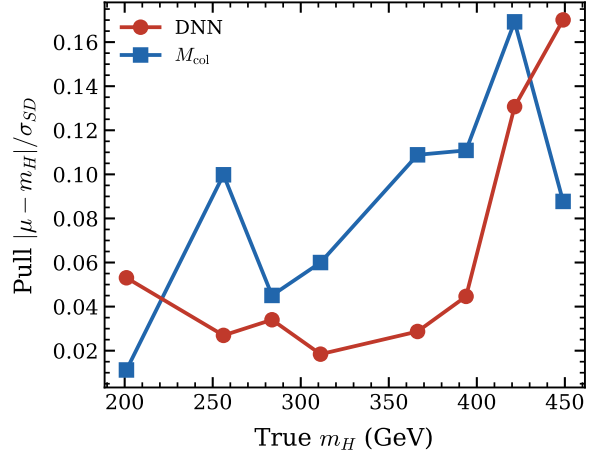
In this work, we have investigated the sensitivity to lepton-flavor-violating (LFV) Higgs decays, $H \rightarrow \mu\tau_e$, within the framework of a Type-III Two-Higgs-Doublet Model. By recasting the 13 TeV CMS search with 35.9 fb^{-1} of integrated luminosity using fast detector simulation, we have demonstrated that modern machine learning techniques can significantly enhance the discovery potential for heavy LFV Higgs bosons in the 200–450 GeV mass range. Our analysis yields three primary conclusions:

First, we established that a DNN-based classifier provides a substantial gain in sensitivity compared to the traditional collinear mass (M_{col}) selection. By optimizing the score threshold independently for each mass hypothesis, we achieved a 36–46% reduction in the expected 95% CL upper limits on the signal cross-section. This improvement is robust across both 0-jet and 1-jet categories, with the most pronounced gains occurring in the high-mass regime where the boosted kinematics of the signal are most distinct from SM backgrounds.

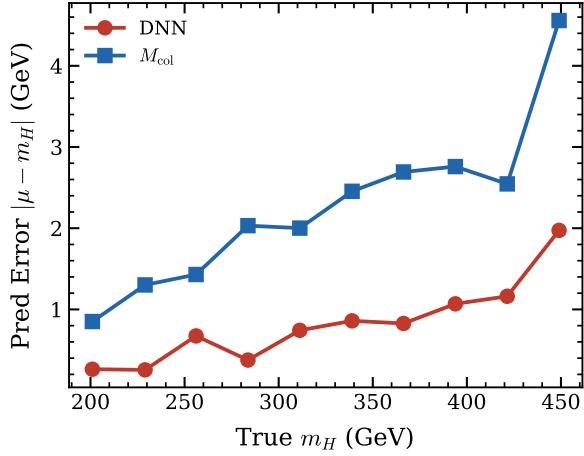
Second, we applied SHAP-based interpretability analysis to interpret the classifier’s decisions. This analysis identified the visible mass, m_{vis} , as one of the main discriminating features. We demonstrate that supplementing the baseline analysis with a simple, mass-dependent cut ($m_{\text{vis}} < f \cdot m_H$) captures a significant fraction of the DNN’s performance. This result is particularly impactful for experimental implementation, as it provides a physically intuitive and easily verifiable refinement to existing search strategies without



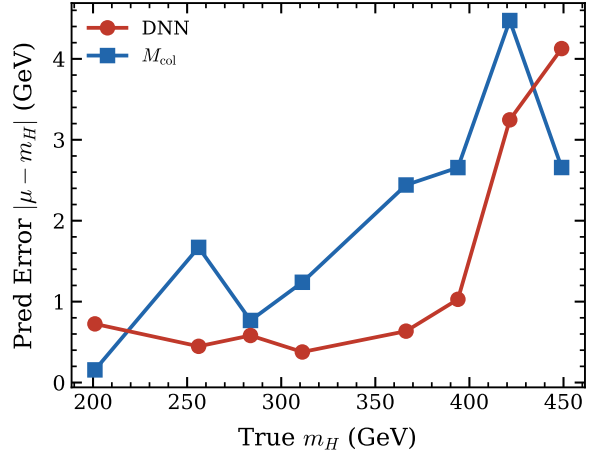
(a) Pull, 0-jet



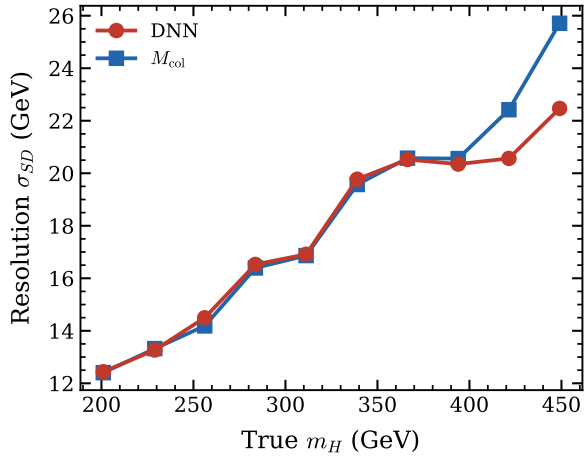
(b) Pull, 1-jet



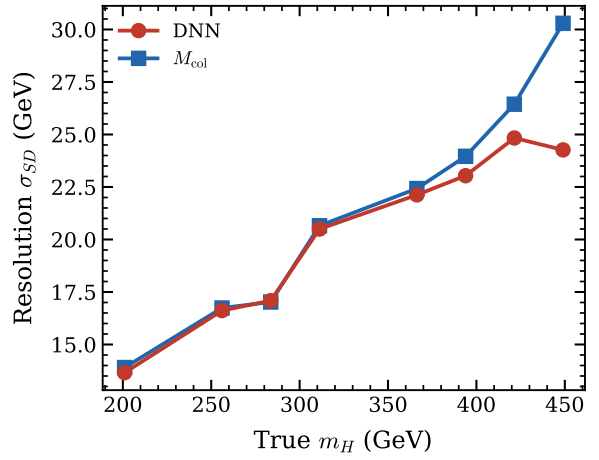
(c) Prediction error, 0-jet



(d) Prediction error, 1-jet



(e) Resolution, 0-jet



(f) Resolution, 1-jet

FIG. 11: Mass reconstruction performance of the DNN regressor compared to M_{col} . The normalized pull $(\mu - m_H)/\sigma_{SD}$ (top row), prediction error $|\mu - m_H|$ (middle row), and resolution σ_{SD} (bottom row) are shown as a function of the true signal mass m_H for the 0-jet (left) and 1-jet (right) channels.

requiring a full multivariate infrastructure.

Third, we addressed the intrinsic systematic prediction error of the collinear mass approximation through deep regression. The DNN regressor successfully mitigates the mass prediction bias of M_{col} throughout the majority of the explored mass range, maintaining an absolute prediction error below 1 GeV for signals up to 400 GeV. The resulting stability in the normalized pull distributions confirms that the network effectively leverages the full event topology to recover information lost to the collinear assumption.

While the present analysis relies on fast detector simulation and the leptonic τ decay mode only, the consistency of the improvements across multiple metrics and both jet categories provides a compelling case for adopting these techniques in dedicated experimental analyses. The analogous decay channel $H \rightarrow \tau e$ is expected to benefit from the same DNN-based enhancements, and extending this framework to that channel is a natural next step. Subsequent iterations of this analysis would also benefit from a full treatment of systematic uncertainties, the inclusion of NLO QCD corrections, and the extension to the hadronic τ decay mode. The m_{vis} -based simplified selection identified in this work offers in particular a concrete and immediately applicable refinement to the standard M_{col} strategy for future LFV Higgs searches at the LHC.

ACKNOWLEDGMENTS

A. F. was supported by funding from the Center for Higher Education Funding and Assesment (PPAPT), Ministry of Higher Education, Science and Technology of Republic Indonesia, and also from Indonesia Endowment Fund for Education Agency (LPDP) as well as Indonesian Education Scholarship (BPI) under funding ID 202209092458. R.P. was supported by Direktorat Penelitian dan Pengabdian kepada Masyarakat, Direktorat Jenderal Riset dan Pengembangan, Kementerian Pendidikan Tinggi, Sains dan Teknologi Republik Indonesia with contract number 7939/LL4/PG/2025; III/LPPM/ 2025-06/154-PE and 125/C3/DT.05.00/PL/2025. F. T. A. and B. E. G. are supported by PPMI KK FMIPA ITB 2026 with contract number 062/IT1.C02/SK-DA/2026.

-
- [1] ATLAS Collaboration, *Phys. Lett. B* **716**, 1 (2012), [arXiv:1207.7214 \[hep-ex\]](#).
 - [2] CMS Collaboration, *Phys. Lett. B* **716**, 30 (2012), [arXiv:1207.7235 \[hep-ex\]](#).
 - [3] G. C. Branco, P. M. Ferreira, L. Lavoura, M. N. Rebelo, M. Sher, and J. P. Silva, *Phys. Rept.* **516**, 1 (2012), [arXiv:1106.0034 \[hep-ph\]](#).
 - [4] T. D. Lee, *Phys. Rev. D* **8**, 1226 (1973).
 - [5] A. Arhrib, Y.-W. Cheng, and O. C. W. Kong, *EPL* **101**, 31003 (2013), [arXiv:1208.4669 \[hep-ph\]](#).
 - [6] A. Goudelis, O. Lebedev, and J.-h. Park, *Phys. Lett. B* **707**, 369 (2012), [arXiv:1111.1715 \[hep-ph\]](#).

- [7] E. Arganda and M. J. Herrero, *Phys. Rev. D* **73**, 055003 (2006), arXiv:hep-ph/0510405.
- [8] K. Agashe and R. Contino, *Phys. Rev. D* **80**, 075016 (2009), arXiv:0906.1542 [hep-ph].
- [9] A. Azatov, M. Toharia, and L. Zhu, *Phys. Rev. D* **80**, 035016 (2009), arXiv:0906.1990 [hep-ph].
- [10] A. J. Buras, B. Duling, and S. Gori, *JHEP* **09**, 076, arXiv:0905.2318 [hep-ph].
- [11] R. Harnik, J. Kopp, and J. Zupan, *JHEP* **03**, 026, arXiv:1209.1397 [hep-ph].
- [12] Y. Omura, E. Senaha, and K. Tobe, *JHEP* **05**, 028, arXiv:1502.07824 [hep-ph].
- [13] R. Primulando and P. Uttayarat, *JHEP* **05**, 055, arXiv:1612.01644 [hep-ph].
- [14] G. Aad *et al.* (ATLAS), *JHEP* **07**, 166, arXiv:2302.05225 [hep-ex].
- [15] A. M. Sirunyan *et al.* (CMS), *Phys. Rev. D* **104**, 032013 (2021), arXiv:2105.03007 [hep-ex].
- [16] CMS Collaboration, *Phys. Lett. B* **749**, 337 (2015), arXiv:1502.07400 [hep-ex].
- [17] ATLAS Collaboration, *Eur. Phys. J. C* **77**, 70 (2017), arXiv:1508.03372 [hep-ex].
- [18] A. Hayrapetyan *et al.* (CMS), *Phys. Rev. D* **108**, 072004 (2023), arXiv:2305.18106 [hep-ex].
- [19] G. Aad *et al.* (ATLAS), *Phys. Lett. B* **801**, 135148 (2020), arXiv:1909.10235 [hep-ex].
- [20] A. M. Sirunyan *et al.* (CMS), *JHEP* **03**, 103, arXiv:1911.10267 [hep-ex].
- [21] P. Baldi, K. Cranmer, T. Faucett, P. Sadowski, and D. Whiteson, *Eur. Phys. J. C* **76**, 235 (2016), arXiv:1601.07913 [hep-ex].
- [22] D. Guest, K. Cranmer, and D. Whiteson, *Ann. Rev. Nucl. Part. Sci.* **68**, 161 (2018), arXiv:1806.11484 [hep-ex].
- [23] K. Albertsson *et al.*, *J. Phys. Conf. Ser.* **1085**, 022008 (2018), arXiv:1807.02876 [physics.comp-ph].
- [24] M. Feickert and B. Nachman, A living review of machine learning for particle physics (2021), arXiv:2102.02770 [hep-ph].
- [25] P. Baldi, P. Sadowski, and D. Whiteson, *Phys. Rev. Lett.* **114**, 111801 (2015), arXiv:1410.3469 [hep-ph].
- [26] P. Bärtzchi, C. Galloni, C. Lange, and B. Kilminster, *Nucl. Instrum. Meth. A* **929**, 29 (2019), arXiv:1904.04924 [hep-ex].
- [27] A. Tumasyan *et al.* (CMS), *Eur. Phys. J. C* **83**, 562 (2023), arXiv:2204.12957 [hep-ex].
- [28] S. Lundberg and S.-I. Lee, A unified approach to interpreting model predictions (2017), arXiv:1705.07874 [cs.AI].
- [29] H. Georgi and D. V. Nanopoulos, *Phys. Lett. B* **82**, 392 (1979).
- [30] J. de Favereau, C. Delaere, P. Demin, A. Giammanco, V. Lemaître, A. Mertens, and M. Selvaggi (DELPHES 3), *JHEP* **02**, 057, arXiv:1307.6346 [hep-ex].
- [31] J. Alwall, R. Frederix, S. Frixione, V. Hirschi, F. Maltoni, O. Mattelaer, H. S. Shao, T. Stelzer, P. Torrielli, and M. Zaro, *JHEP* **07**, 079, arXiv:1405.0301 [hep-ph].
- [32] T. Sjöstrand, S. Ask, J. R. Christiansen, R. Corke, N. Desai, P. Ilten, S. Mrenna, S. Prestel, C. O. Rasmussen, and P. Z. Skands, *Comput. Phys. Commun.* **191**, 159 (2015), arXiv:1410.3012 [hep-ph].
- [33] E. Conte, B. Fuks, and G. Serret, *Comput. Phys. Commun.* **184**, 222 (2013), arXiv:1206.1599 [hep-ph].
- [34] E. Conte, B. Dumont, B. Fuks, and C. Wymant, *Eur. Phys. J. C* **74**, 3103 (2014), arXiv:1405.3982 [hep-ph].
- [35] K. Hagiwara, T. Li, K. Mawatari, and J. Nakamura, *Eur. Phys. J. C* **73**, 2489 (2013), arXiv:1212.6247 [hep-ph].
- [36] M. Abadi, A. Agarwal, P. Barham, E. Brevdo, Z. Chen, C. Citro, G. S. Corrado, A. Davis, J. Dean, M. Devin,

- S. Ghemawat, I. Goodfellow, A. Harp, G. Irving, M. Isard, Y. Jia, R. Jozefowicz, L. Kaiser, M. Kudlur, J. Levenberg, D. Mané, R. Monga, S. Moore, D. Murray, C. Olah, M. Schuster, J. Shlens, B. Steiner, I. Sutskever, K. Talwar, P. Tucker, V. Vanhoucke, V. Vasudevan, F. Viégas, O. Vinyals, P. Warden, M. Wattenberg, M. Wicke, Y. Yu, and X. Zheng, [TensorFlow: Large-scale machine learning on heterogeneous systems](#) (2015), software available from tensorflow.org.
- [37] N. Srivastava, G. Hinton, A. Krizhevsky, I. Sutskever, and R. Salakhutdinov, [Journal of Machine Learning Research](#) **15**, 1929 (2014).
- [38] S. Ioffe and C. Szegedy, in *Proceedings of the 32nd International Conference on Machine Learning*, Proceedings of Machine Learning Research, Vol. 37, edited by F. Bach and D. Blei (PMLR, Lille, France, 2015) pp. 448–456.
- [39] G. Cowan, K. Cranmer, E. Gross, and O. Vitells, [Eur. Phys. J. C](#) **71**, 1554 (2011), [Erratum: [Eur.Phys.J.C](#) 73, 2501 (2013)], [arXiv:1007.1727 \[physics.data-an\]](#).